World Scientific
www.worldscientific.com

ON NONLINEAR RESPONSE NEAR-HALF NATURAL FREQUENCY OF ELECTROSTATICALLY ACTUATED MICRORESONATORS

DUMITRU I. CARUNTU[*,‡] and MARTIN W. KNECHT[†]

[*]*Mechanical Engineering Department*
University of Texas-Pan American
Edinburg, Texas 78541, U.S.A.

[†]*South Texas College, Engineering Department*
McAllen, TX 78501, U.S.A.
[‡]*caruntud@utpa.edu*
[‡]*caruntud2@asme.org*
[‡]*dcaruntu@yahoo.com*

This paper deals with the nonlinear response of electrostatically actuated cantilever beam microresonators near-half natural frequency. A first-order fringe correction of the electrostatic force, viscous damping, and Casimir effect are included in the model. Both forces, electrostatic and Casimir, are nonlinear. The dynamics of the resonator is investigated using the method of multiple scales (MMS) in a direct approach of the problem. The reduced order model (ROM) method, based on Galerkin procedure, is used as well. Steady-state motions are found. Numerical simulations are conducted for uniform microresonators. The influences of damping, actuation, and fringe effect on the resonator response are reported.

Keywords: Nonlinear dynamics; MEMS resonators; electrostatic actuation.

Nomenclature

Constants

$\varepsilon_0 = 8.854 \times 10^{-12}$ C^{2}N^{-1}m^{-2} Permittivity of free space
$\hbar = 1.055 \times 10^{-34}$ J $\cdot$ s   Dirac constant
$c = 2.998 \times 10^8$ m $\cdot$ s^{-1} Speed of light
$\mu = 1.85 \times 10^{-5}$ kg $\cdot$ m^{-1}s^{-1} Dynamic coefficient of air at 25°C

[‡]Corresponding author.

Parameters

A	Resonator cross-sectional area
A^*	Dimensionless cross-sectional area
b	Damping coefficient
E	Young's modulus
f	Fringe correction parameter
g	Initial resonator gap
h	Resonator thickness
I	Moment of inertia
I^*	Dimensionless moment of inertia
ℓ	Beam length
M	Molar mass of gas
P	Air pressure
Q	Quality factor
T	Temperature
V	Voltage
W	Resonator width
α	Casimir parameter
δ	Excitation parameter
ω_k	Natural frequency
Ω	Excitation frequency

Variables

a	Resonator amplitude
t	Dimensional time
$u(z)$	Dimensionless beam displacement
$w(x)$	Dimensional beam displacement
x	Dimensional position along beam
z	Dimensionless position along beam
τ	Dimensionless time

1. Introduction

Microelectromechanical (MEMS) resonator systems such as microbeams and microplates are used in a variety of applications. Yet, they are mostly used as linear resonators. Nonlinearities play a significant role at micron scale. Therefore, a better understanding of the dynamics of nonlinear systems is essential. Nonlinearities arise from a number of sources such as large deflections (geometric nonlinearities), squeeze-film damping, electrostatic actuation, and intermolecular surface forces such as Casimir or van der Waals[1] present at micron and submicron scales. A model including Casimir effect and a first-order fringe effect has been reported in the literature.[2] Electrostatic excitation is produced by a fluctuating voltage between

a microcantilever resonator and a ground plate, and leads to parametric coefficients in both linear and nonlinear terms of the equation of motion. A similar investigation has been conducted for a parametrically excited comb drive system.[3]

Electrostatic actuation creates a variety of nonlinear parametric resonances depending on system parameters, excitation frequency, and excitation voltage. Various bifurcations, in which the frequency of excitation has been used as the bifurcation parameter, have been reported in the literature. Understanding the nature of parametric excitations is of general interest. Parametric excitations can be used to design devices such as mass sensors,[4,5] microscopy probes,[6,7] filters,[8,9] and resonators.[9−13] In addition, the stability of these systems and the types of non-linearities that occur are highly sensitive to physical parameters, initial amplitude, and excitation frequency.[3,9−13] It is then important to identify bifurcation parameters and bifurcation points in order to design and control systems under parametric excitation. Bifurcation analyses have been reported in literature for parametrically excited systems, mainly for discrete comb drive systems.[3,14] Parametric excitations in a cantilevered beam coupled to an electrical system via a piezoelectric patch have been used for energy harvesting.[15] It has been found that there was an optimal value for the electromechanical coupling terms in order to maximize the output voltage of the harvester. Regarding harvester's sensitivity, a critical value for excitation forces below which oscillations did not occur has been reported. This value has been showed to be dependent on the electromechanical coupling term. A double-sided electromechanically driven nanotube resonator taking into account the van der Waals force has been investigated as well.[16] An energy-based method has been used to create analytical relationships for the steady-state amplitude of the nanotube as a function of driving frequency and excitation voltage. In addition, an analytical relationship for the resonant pull-in voltage has been developed.

This paper investigates the influence of nonlinearities resulting from parametric electrostatic excitation and Casimir effect on the response of cantilever microbeams near-half natural frequency. The model of the microcantilever resonator is developed using the Euler−Bernoulli hypothesis of thin beams. The partial differential equation of motion is obtained using Hamilton's principle. Then, the method of multiple scales (MMS) is directly applied to the partial differential equation of motion to obtain the frequency−amplitude relationship of the microcantilever resonator. To the best of our knowledge an analysis including fringe and Casimir effects has not been conducted for soft excitations of continuous microsystems such as microcantilever resonators. Most of the analysis in literature investigates pull-in stability and amplitude−frequency relations or finds limit cycles and time responses of such systems.[2,17−19]

2. System Model

This section describes the development of the model being used in the investigation of microcantilever resonators. The equation of motion of the resonator is based on Euler−Bernoulli theory for thin beams. Subsequent sections discuss the effects being

considered in the model which include: (1) the electrostatic force used to actuate the resonator, (2) damping forces, and (3) nanoscale surface forces (Casimir effect).

2.1. *Partial-differential equation of motion*

Consider a flexible cantilever beam suspended over a grounded substrate. The beam is electrostatically actuated by applying a potential difference between the cantilever and the underlying plate. In addition to the electrostatic force, viscous damping and Casimir effect are considered. The length of the beam is relatively large compared to the underlying gap. Thus the slope of the resonator is relatively small. Therefore, Euler−Bernoulli hypothesis holds. Using generalized Hamilton's principle, the boundary value problem of electrostatically actuated microcantilever resonators (Fig. 1), is as follows

$$\begin{cases} \rho A(x)\dfrac{\partial^2 w}{\partial t^2} + \dfrac{\partial^2}{\partial x^2}\left(EI(x)\dfrac{\partial^2 w}{\partial x^2}\right) - R(x) = 0 \\[4mm] w(0) = \dfrac{\partial w}{\partial x}(0) = \dfrac{\partial^2 w}{\partial x^2}(\ell) = \dfrac{\partial^3 w}{\partial x^3}(\ell) = 0\,, \end{cases} \tag{1}$$

where $w = w(x,t)$ is the transverse displacement of the beam, x longitudinal coordinate, ℓ beam's length, E Young's modulus, $A(x)$ cross-sectional area, $I(x)$ cross-sectional moment of inertia, and ρ material density. The electrostatic force F_e, Casimir force F_c, and damping force F_d were considered in the development of the nonconservative forces as follows:
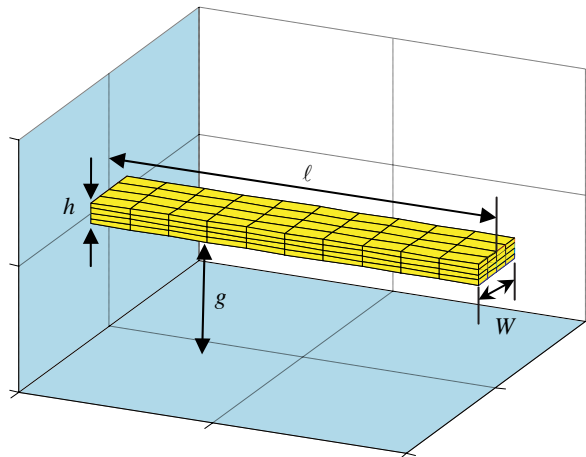
$$R(x) = F_e + F_c - F_d. \tag{2}$$

Fig. 1. Uniform cantilever resonator.

2.2. *Electrostatic Force and Fringe Effect*

The actuation force is produced by applying a potential difference across the upper beam and underlying conducting plate. This force is commonly modeled using the parallel plate equation for capacitors calculated by assuming infinitely large plates with no edge

$$F_e' = \frac{\varepsilon_0 W}{2} \frac{V^2}{(g-w)^2},$$

(3)

where $\varepsilon_0 = 8.854 \times 10^{-12}\,\mathrm{C^2 N^{-1} m^{-2}}$ is the permittivity of free space, W is the beam width, g is the initial gap between the beam and ground electrode, and $V(t)$ is the applied voltage. This is a reasonable treatment of the electrostatic force under many circumstances where the width of the beam is large with respect to the gap and with small deflections relative to the gap. When the beam's gap-to-width (g/W) ratio is less than 0.6 and thickness-to-width (h/W) ratio is less than 0.2, the parallel plate approximation is typically used.[20] This approximation may not be sufficient, however. When numerically calculated values of the parallel plate capacitance are compared with values using the infinite plate approximation (3), it is found that the beam must be wide and thin with a gap-to-width ratio of $g/W < 0.01$ and a thickness-to-width ratio of $h/W < 0.1$ to have a deviation of 6% or less.[21] If a narrower or thicker beam is to be considered, the parallel plate treatment of the force becomes insufficient. The inaccuracies arise from fringing effects that occur due to the finite width and thickness of the beam. The fringe effect accounts for the field lines that curve from the edge of one plate to another and are outside the volume between plates. Therefore, the electrostatic force is larger than predicted by the parallel plate approximation. To include the effects of electrostatic fringe effect, a corrective factor $\mathcal{F}(g,h,w)$ to the idealized parallel plate formulation is considered as follows:

$$F_e = F_e' \cdot \mathcal{F}(g,h,w).$$

(4)

The fringe correction factor $\mathcal{F}$ depends only on the geometry of the beam. In the case of an idealized parallel-plate approximation given by Eq. (3), $\mathcal{F} = 1$. Several expressions are available in literature dedicated to fringe correction factors $\mathcal{F}$. These expressions are appropriate under certain circumstances. One of the earliest formulations of the fringe correction factor $\mathcal{F}$ is Palmer's formula[22]

$$\mathcal{F} = 1 + \frac{2}{\pi} \frac{g}{W} \left(1 + \ln\left(\pi \frac{g}{W}\right)\right).$$

(5)

This correction factor accounts for a large but finite plate width. It does not include finite thickness corrections. Therefore, this correction factor would be most appropriately used when working with thin and wide beams but an improvement over the infinite plate approximation. When the capacitance using the Palmer formulation (5) is compared to numerically calculated values, a deviation of 4% or less is obtained with $g/W < 0.04$ and $h/W < 0.1$.[21] Meijs−Fokkema developed the fringe correction

factor formula[23] as follows

$$\mathcal{F} = 1 + 0.77\frac{g}{W} + 1.06\Big(\frac{g}{W}\Big)^{0.75} + 1.06\Big(\frac{gh}{W^2}\Big)^{0.5}. \tag{6}$$

This formulation accounts for both a finite plate width and thickness. In addition, it is valid for narrower beams. When the capacitance using the Meijs–Fokkema formulation (6) is compared with the numerically calculated values, a deviation of 5% or less is obtained with $g/W < 4$.[21] Batra *et al.*[21] numerically developed a fringe correction factor formula taking into account both finite width and thickness

$$\mathcal{F} = 1 + 0.36\frac{g}{W} + 0.85\Big(\frac{g}{W}\Big)^{0.76} + 2.5\Big(\frac{gh}{W^{1.316}}\Big)^{0.76}. \tag{7}$$

Their equation was developed by first assuming that the fringe correction factor function could be described in the same form as the Meijs–Fokkema correction (6). They then numerically computed the capacitance per unit length of a thick and narrow beam for different values of width and thickness. The resulting data was then least square fitted to the assumed function giving the correction in Eq. (7). This approximation performs even better with deviations from numerically calculated values of less than 2% for $g/W < 10$.

Previous formulations ((5)−(7)) determined the electrostatic force per unit length on a beam correcting for fringe effects due to either finite width or thickness. There is an underlying assumption that the gap-to-length ratio of the beams are relatively small (on the order of 10^{-2}−10^{-3}) for each formulation in Eqs. (5)−(7) and, therefore, the deflections of the beam should be small. An approximation is made assuming the beam to be locally parallel.[24] If the gap-to-length ratio is larger, the curvature of the beam may need to be taken into account. Therefore, a parallel plate approximation is not appropriate. Krylov *et al.*[24] formulated a correction to the electrostatic force assuming larger gaps taking into account the curvature of a beam

$$\mathcal{F} = 1 - \frac{\big(\frac{g}{\ell}\big)^2}{3g^2}\left[\Big(\frac{\partial w}{\partial x}\Big)^2 + 2(g-w)\frac{\partial^2 w}{\partial x^2}\right]. \tag{8}$$

The function was developed using a straightforward perturbation method by truncating the terms higher than second order. Results for terms up to fourth order were also presented in Ref. 24 which contained more complicated higher-order partial derivatives. This formulation (8), however, is limited to wide thin beams. As long as the beam is sufficiently wide, the electric field pressure calculated by Eq. (8) has a deviation of less than 1% for gap-to-length ratios of $g/\ell < 0.5$.

For the model being developed in this paper, the Palmer approximate formula is used considering only the first-order fringing correction. This gives an electrostatic force per unit length along the beam as

$$F_e = \frac{\varepsilon_0 W}{2}\,\frac{V(t)^2}{(g-w)^2}\left(1 + 0.65\frac{(g-w)}{W}\right). \tag{9}$$

Equation (9) allows an investigation of how the fringe corrections can affect the characterization of nonlinearities within a system.

A typical strategy for actuating a microresonator is by applying a voltage that consists of both a polarizing DC voltage on top of a fluctuating AC voltage such that

$$V(t) = V_p + V_0 \cos(\Omega t), \tag{10}$$

where V_p is the DC component, V_0 is the AC amplitude, and Ω is the frequency of the AC voltage. The voltage is squared to determining the electrostatic actuation force (9). The square of the voltage can be written as

$$V(t)^2 = V_p^2 + \frac{V_0^2}{2} + 2V_p V_0 \cos(\Omega t) + \frac{V_0^2}{2} \cos(2\Omega t). \tag{11}$$

The voltage (11) and, therefore, the actuating force can be characterized as having three components. A static component due to the first two terms $V_p^2 + V_0^2/2$, a first harmonic component due to the third term $2V_p V_0 \cos(\Omega t)$, and a second harmonic component due to the last term $0.5 \cdot V_0^2 \cos(2\Omega t)$. By adjusting the DC and AC components of the voltage, one can influence which of the harmonics dominates in the actuation of the system. If there is no AC voltage applied, $V_0 = 0$, then a static actuating force is applied.[1,19,25,26] If the polarizing voltage is much larger than the AC voltage, $V_p \gg V_0$, as considered in many cases,[19] then the second harmonic can be neglected since it is sufficiently small. The resonator is then influenced by only the first harmonic of the voltage on top of a static deflection.

This paper investigates the case in which there is no DC polarizing voltage, $V_p = 0$, with only the AC voltage present. In this case, it is first noticed from Eq. (11) that even when the polarizing voltage is neglected, the AC voltage will still contribute to the static voltage component. Second, the first harmonic of the applied voltage is zero with only the second harmonic contributing such that

$$V(t)^2 = \frac{V_0^2}{2} + \frac{V_0^2}{2} \cos(2\Omega t). \tag{12}$$

If Eq. (9) is then Taylor expanded with respect to the beam deflection w, then it can be further illustrated how the electrostatic force induces a combination of pure harmonic and parametric excitations to the resonator

$$F_e = \frac{\varepsilon_0}{2} V^2(t) \left[\left(\frac{W + 0.65g}{g^2} \right) + \left(\frac{2W + 0.65g}{g^3} \right) w + \left(\frac{3W + 0.65g}{g^4} \right) w^2 \right.$$
$$\left. + \left(\frac{4W + 0.65g}{g^5} \right) w^3 \right] \tag{13}$$

A similar approach has been used to actuate a comb-finger resonator.[4,5]

2.3. *Damping forces*

A variety of sources can contribute to energy losses within a micromechanical system. These losses may include air damping, internal friction, support loss, and

thermoelastic damping. Depending on the environment in which the MEMS device is operating, different loss mechanisms become dominant. When the device is in an ultra low pressure environment, losses due to air damping are not significant and structural losses are dominant. At higher pressures, however, the opposite is true. The air damping effects are dominant.

For an oscillating beam near a fixed surface, the air damping can consist of two components. The first is due to viscous flow as the beam moves through the air. The force per unit length due to viscous damping is described by

$$F_d = b\frac{\partial w}{\partial t}, \tag{14}$$

where b is the coefficient of viscous damping per unit length.[27]

The second source of air damping is due to air being pushed out or sucked into the region between the oscillating beam and fixed wall. This so-called squeeze film damping can be approximated as a type of restoring force caused by the compression of air between plates and is sometimes referred as elastic damping. The force per unit length due to elastic damping is described by

$$F_e = k_e w; \quad k_e = \frac{8\ell W P_a}{\pi^2 g}, \tag{15}$$

where k_e is the coefficient of elastic damping (given here for a narrow beam) and P_a is the air pressure.[27] The type of air damping that dominates within a system, viscous or elastic, depends on the frequency of the oscillator and the surrounding air pressure. At low frequencies, the air does not get significantly compressed and viscous damping is a larger influence than elastic. If the oscillation frequencies are large, however, the air does not have time to escape the cavity between the plates and is compressed causing elastic damping to be a larger influence.[27]

Pressure affects how damping influences a system as well. Depending on the air pressure, the effects of viscous damping falls into four regimes: intrinsic, molecular, intermediate, and viscous.[28,29] The intrinsic region $(<1\,\text{Pa})$[29] represents extremely low pressures where air damping becomes negligible and structural damping is the primary source of damping. The molecular region $(1-66\,\text{Pa})$[28] damping is caused by collisions with individual molecules and can be analytically describes by applying the kinetic theory of gases. The intermediate region $(66-6600\,\text{Pa})$[28] is described by Stokes' damping,[29] and the viscous region $(>6600\,\text{Pa})$ is described by applying Reynolds equation for a continuous flow, which is a special case of the Navier−Stokes equation in the limit of small Reynolds numbers.

If the pressure at which the resonator operates remains in the viscous regime, the Reynolds equation can be applied directly to the case of a long and narrow plate. This gives an expression for the quality factor based on the geometry of the plate,[27] in which the quality factor is a dimensionless quantity that describes the rate of energy

loss by a system

$$Q = \frac{\pi^4 \rho A \omega g^3}{96 \mu \ell W^3}.$$ (16)

This would imply that viscous damping is independent of air pressure. This has been experimentally shown to be relatively good approximation near atmospheric pressures.[27]

For the other pressure regions, a pressure dependence on the quality factor is observed. Within the intermediate region and low-pressure viscous region, the quality factor is derived using the Navier−Stokes equation by approximating a beam as a string of spheres with a radius equal to the width of the beam.[30] The quality factor is found to be proportional to $1/\sqrt{P}$ in this case. In cases in which the resonator is operating in a rarefied environment, a molecular model is used based on the kinetic theory of gasses and the interaction of gas molecules and oscillating plate.[28] The quality factor is found to be proportional to $1/P$ in this case.

In order to characterize the relative influences of viscous and elastic dampings, the squeeze number σ is considered. The number σ is derived via the Reynolds equation[31]

$$\sigma = \frac{12 \mu S^2 \omega}{P_a g^2},$$ (17)

where μ is the dynamic coefficient of viscosity, S is the characteristic size of the system (beam width in our case), P_a is the absolute air pressure, and g is the gap width. For small squeeze numbers, viscous damping is dominant while at large squeeze numbers, elastic damping is dominant. At a squeeze number of approximately $\sigma = 10$ (the cut-off squeeze number), the viscous and elastic forces are equal.[27] For example, if we consider a microcantilever of $300\,\mu$m length, $20\,\mu$m width, $2\,\mu$m thickness, $8\,\mu$m gap, 350 quality factor Q, $2330\,$kg/m^3 density, and $169\,$GPa Young modulus, at the lower end of the viscous regime ($6600\,$Pa) and consider oscillations near primary resonance ($30\,$kHz), the squeeze number is found to be small $\sigma = 0.04$. This means the dominant source of air damping is viscous and the elastic air damping is negligible.[27] The model being constructed in this paper will be considered within this regime (16).

It is convenient to consider the effects of damping and the quality factor in terms of a damping coefficient for modeling purposes. For viscous air dampings, the relationship between the quality factor and damping coefficient is given by[10]

$$b = \frac{\rho A \omega}{Q}.$$ (18)

By substituting Eq. (16) into Eq. (18), the viscous damping coefficient is found to be

$$b = \frac{96 \mu \ell W^3}{\pi^4 g^3}.$$ (19)

2.4. *Casimir force*

When the separation of surfaces is larger than 20 nm and less than 1000 nm, Casimir effects occur.[2] In this work, such gap distances are considered. The Casimir force per unit length along the beam is given by[32]

$$F_c = \frac{\pi^2 \hbar c W}{240(g-w)^4},$$ (20)

where $\hbar = 1.055 \times 10^{-34}$ J s is Planck's constant divided by 2π and $c = 2.998 \times 10^8$ m s^{-1} is the speed of light.

3. Dimensionless Equation

Dimensionless variables are now introduced

$$u = \frac{w}{g}, \quad z = \frac{x}{\ell}, \quad \tau = t \frac{1}{\ell^2} \sqrt{\frac{EI_0}{\rho A_0}},$$ (21)

where $u, z,$ and τ are the dimensionless beam displacement, dimensionless longitudinal coordinate, and dimensionless time, respectively. The dimensionless cross-sectional area A^* and inertia I^* are $A^* = A/A_0$ and $I^* = I/I_0$, respectively, where A_0 and I_0 are reference cross-sectional area and moment of inertia. Substituting Eq. (21) into Eq. (1), one obtains the dimensionless boundary value problem

$$\begin{cases} A^* \dfrac{\partial^2 u}{\partial \tau^2} + \dfrac{\partial^2}{\partial z^2}\left(I^* \dfrac{\partial^2 u}{\partial z^2} \right) = -b^* \dfrac{\partial u}{\partial \tau} + \dfrac{\alpha}{(1-u)^4} + \dfrac{\delta}{(1-u)^2} V^2(\tau) \\ \qquad\qquad\qquad\qquad\qquad + f \dfrac{\delta}{(1-u)} V^2(\tau) \\ u(0) = \dfrac{\partial u}{\partial z}(0) = \dfrac{\partial^2 u}{\partial z^2}(1) = \dfrac{\partial^3 u}{\partial z^3}(1) = 0, \end{cases}$$ (22)

where

$$\alpha = \frac{\pi^2 \hbar c W \ell^4}{240 g^5 EI_0}, \quad \delta = \frac{\varepsilon_0 W \ell^4}{2g^3 EI_0} V_0^2, \quad f = \frac{0.65g}{W}, \quad b^* = b \frac{\ell^2}{\sqrt{\rho A_0 EI_0}}.$$ (23)

The dimensionless parameters $\alpha, \delta, f,$ and b^* of Eq. (23) track the influence of Casimir effect, electrostatic excitation amplitude, fringe effect, and damping, respectively. In addition, $V(\tau)$ is the dimensionless voltage and V_0 the reference voltage. It will also be convenient to introduce a dimensionless frequency ω^*, which follows from the dimensionless time in Eq. (21) as

$$\omega^* = \omega \ell^2 \sqrt{\frac{\rho A_0}{EI_0}}.$$ (24)

Substituting the dimensionless damping coefficient, Eqs. (23) and (24), into Eq. (18), the quality factor can be related to dimensionless damping parameter as follows

$$b^* = \frac{\omega^*}{Q}. \tag{25}$$

4. Direct Approach using the Method of Multiple Scales (MMS)

Consider parameters α, δ, f, and b^* to be small. This corresponds to weak influences of the Casimir effect, excitation force, fringe correction, and damping. Expanding around $u = 0$ the right-hand side of Eq. (22), retaining the terms up to the third power of u, and setting all these terms to a slow scale by multiplying them by ε a small dimensionless bookkeeping parameter, one obtains

$$A^* \frac{\partial^2 u}{\partial \tau^2} + \frac{\partial^2}{\partial z^2} \left(I^* \frac{\partial^2 u}{\partial z^2} \right)$$
$$= -\varepsilon b^* \frac{\partial u}{\partial \tau} + \varepsilon \alpha [1 + 4u + 10u^2 + 20u^3]$$
$$+ \varepsilon \delta [(1 + f) + (2 + f)u + (3 + f)u^2 + (4 + f)u^3] V^2(\tau). \tag{26}$$

The MMS is then applied. A first-order expansion of the dimensionless displacement u is then considered

$$u(z, \tau, \varepsilon) = u_0(z, T_0, T_1) + \varepsilon \cdot u_1(z, T_0, T_1), \tag{27}$$

where $T_0 = \tau$ is a fast time scale and $T_1 = \varepsilon \cdot \tau$ is a slow time scale. The time derivatives then become $\partial/\partial \tau = D_0 + \varepsilon \cdot D_1$ where $D_n = \partial/\partial T_n$. Replacing Eq. (27) and the time derivatives into Eq. (26) and equating coefficients of like powers of ε, the following two approximation problems result:

$$\text{Order } \varepsilon^0 : \begin{cases} A^* D_0^2 u_0 + \dfrac{\partial^2}{\partial z^2} \left(I^* \dfrac{\partial^2 u_0}{\partial z^2} \right) = 0 \\[4mm] u_0(0) = \dfrac{\partial u_0}{\partial z}(0) = \dfrac{\partial^2 u_0}{\partial z^2}(1) = \dfrac{\partial^3 u_0}{\partial z^3}(1) = 0 \end{cases}, \tag{28}$$

$$\text{Order } \varepsilon^1 : \begin{cases} A^* D_0^2 u_1 + \dfrac{\partial^2}{\partial z^2} \left(I^* \dfrac{\partial^2 u_1}{\partial z^2} \right) \\[2mm] \qquad = -2D_0 D_1 u_0 - b^* D_0 u_0 + \alpha[1 + 4u_0 + 10u_0^2 + 20u_0^3] \\[2mm] \qquad\quad + \delta[(1 + f) + (2 + f)u_0 + (3 + f)u_0^2 + (4 + f)u_0^3] V^2(T_0) \\[2mm] u_1(0) = \dfrac{\partial u_1}{\partial z}(0) = \dfrac{\partial^2 u_1}{\partial z^2}(1) = \dfrac{\partial^3 u_1}{\partial z^3}(1) = 0. \end{cases}. \tag{29}$$

The solution u_0 of the zero-order boundary value problem given by Eq. (28) is assumed to be

$$u_0(z, T_0, T_1) = \varphi_(z)[A(T_1)e^{i\omega T_0} + \overline{A}(T_1)e^{-i\omega T_0}], \tag{30}$$

where A and $\overline{A}$ are complex conjugate coefficients depending on the slow time scale T_1. Solving the boundary value problem, the mode shapes $\varphi_k(z)$ and their corresponding natural frequencies ω_k are obtained. The natural modes for uniform cantilevers and cantilevers of varying thickness are reported in the literature.[33,34] The dimensionless voltage is considered as

$$V(\tau) = \cos \Omega^* T_0, \tag{31}$$

where Ω^* is the dimensionless frequency of excitation given by

$$\Omega^* = \Omega l^2 \sqrt{\frac{\rho A_0}{EI_0}}. \tag{32}$$

In the following section, the first-order problem is solved to provide the phase-amplitude evolution.

5. Resonance Near-Half Natural Frequency $\Omega \approx \omega_k/2$

In this section, the resonance when excitation frequency is near half the natural frequency, $\Omega^* \approx \omega_k/2$, is investigated. The nearness of the excitation frequency can be written as

$$2\Omega^* = \omega_k + \varepsilon\sigma, \tag{33}$$

where σ is a detuning parameter. Using Eqs. (31) and (33), the square of the voltage V is given by

$$V^2(T_0) = \frac{1}{2} + \frac{\left(e^{i\omega_k T_0 + i\sigma T_1} + e^{-i\omega_k T_0 - i\sigma T}\right)}{4}. \tag{34}$$

5.1. *Phase–amplitude relationship*

After substituting Eqs. (33) and (34) into Eq. (29), the secular terms are collected and set equal to zero. One can notice that excitation frequencies near-half natural frequency, $\Omega^* \approx \omega_k/2$, give additional secular terms. Once the solvability condition, stating that the right-hand side has to be orthogonal to every solution of the homogenous problem (28), is applied, one obtains

$$-2i\omega_k g_{1kk}A_k' - i\omega_k b^* g_{1kk}A_k + (4\alpha + C_2)g_{1kk}A_k + 3(20\alpha + C_4)g_{3kk}A_k^2\bar{A}_k$$
$$+ \frac{1}{2}C_1 g_{0kk}e^{i\sigma T_1} + C_3 g_{2kk}A_k\bar{A}_k e^{i\sigma T_1} + \frac{1}{2}C_3 g_{2kk}A_k^2 e^{-i\sigma T_1} = 0, \tag{35}$$

where

$$C_1 = \frac{1}{2}(1+f)\delta, \quad C_3 = \frac{1}{2}(3+f)\delta, \tag{36}$$

and A_k' is the derivative of A_k with respect to the slow time scale T_1. The coefficients g_{nkk} are given by

$$g_{nkk} = \langle A^*\varphi_k^n, \varphi_k \rangle = \int_0^1 A^*\varphi_k^n \varphi_k dz. \tag{37}$$

where A^* is the dimensionless cross-section area.

Expressing A_k in polar form

$$A_k = \frac{1}{2} a_k e^{i\beta_k}, \tag{38}$$

and separating the real and imaginary parts, the following amplitude and phase equations result as follows:

$$a_k' = -\frac{b^*}{2} a_k + \left[C_1 \frac{g_{0kk}}{g_{1kk}} + \frac{C_3}{4} \frac{g_{2kk}}{g_{1kk}} a_k^2 \right] \frac{\sin(\sigma T_1 - \beta_k)}{2\omega_k} \tag{39}$$

$$a_k \beta_k' = -\frac{(4\alpha + C_2)}{2\omega_k} a_k - \frac{3(20\alpha + C_4)}{8\omega_k} \frac{g_{3kk}}{g_{1kk}} a_k^3$$

$$- \left[C_1 \frac{g_{0kk}}{g_{1kk}} + \frac{3C_3}{4} \frac{g_{2kk}}{g_{1kk}} a_k^2 \right] \frac{\cos(\sigma T_1 - \beta_k)}{2\omega_k}. \tag{40}$$

Using the following change of variables

$$\gamma_k = \sigma T_1 - \beta_k, \tag{41}$$

Eqs. (46) and (47) become

$$a_k' = -\frac{b^*}{2} a_k + \left[C_1 \frac{g_{0kk}}{g_{1kk}} + \frac{C_3}{4} \frac{g_{2kk}}{g_{1kk}} a_k^2 \right] \frac{\sin \gamma_k}{2\omega_k} \tag{42}$$

$$a_k \gamma_k' = a_k \sigma + \frac{(4\alpha + C_2)}{2\omega_k} a_k + \frac{3(20\alpha + C_4)}{8\omega_k} \frac{g_{3kk}}{g_{1kk}} a_k^3$$

$$+ \left[C_1 \frac{g_{0kk}}{g_{1kk}} + \frac{3C_3}{4} \frac{g_{2kk}}{g_{1kk}} a_k^2 \right] \frac{\cos \gamma_k}{2\omega_k}. \tag{43}$$

Numerical integration of Eqs. (42) and (43) showing steady state for a uniform microresonator is presented in Sec. 6.1.

5.2. *Steady-state solutions*

Steady-state solutions are considered by setting $a_k' = \gamma_k' = 0$. This gives the following set of parametric equations describing the amplitude−frequency relationship

$$\frac{C_3}{4} \frac{g_{2kk}}{g_{1kk}} \frac{\sin \gamma_k}{2\omega_k} a_k^2 - \frac{b^*}{2} a_k + C_1 \frac{g_{okk}}{g_{1kk}} \frac{\sin \gamma_k}{2\omega_k} = 0, \tag{44}$$

$$\sigma = -\frac{4\alpha + C_2}{2\omega_k} - \frac{3(20\alpha + C_4)}{8\omega_k} \frac{g_{3kk}}{g_{1kk}} a_k^2 - \left[C_1 \frac{g_{0kk}}{g_{1kk}} + \frac{3C_3}{4} \frac{g_{2kk}}{g_{1kk}} a_k^2 \right] \frac{1}{a_k} \frac{\cos \gamma_k}{2\omega_k}. \tag{45}$$

Two amplitude solutions result from Eq. (44) as follows

$$a_k = \frac{2}{C_3} \frac{g_{1kk}}{g_{2kk}} \frac{\omega_k}{\sin \gamma_k} b^* \pm \left[\left(\frac{2}{C_3} \frac{g_{1kk}}{g_{2kk}} \frac{\omega_k}{\sin \gamma_k} b^* \right)^2 - \frac{4C_1}{C_3} \frac{g_{0kk}}{g_{2kk}} \right]^{1/2}. \tag{46}$$

Steady-state solutions for a uniform microresonator are presented in Sec. 6.1.

654   *D. I. Caruntu & M. W. Knecht*

5.3. *Stability of steady-state solution*

The stability of steady-state points, given by amplitude and phase (a_0, γ_0), is tested by using the Jacobian of Eqs. (45) and (46)

$$
J = \begin{bmatrix} \dfrac{\partial a'}{\partial a} & \dfrac{\partial a'}{\partial \gamma} \\ \dfrac{\partial \gamma'}{\partial a} & \dfrac{\partial \gamma'}{\partial \gamma} \end{bmatrix}_{(a_0, \gamma_0)}
$$

$$
= \begin{bmatrix} -\dfrac{b^*}{2} + \dfrac{C_3}{4} \dfrac{g_{2kk}}{g_{1kk}} a_k \dfrac{\sin \gamma_k}{\omega_k} & \left(C_1 \dfrac{g_{0kk}}{g_{1kk}} + \dfrac{C_3}{4} \dfrac{g_{2kk}}{g_{1kk}} a_k^2 \right) \dfrac{\cos \gamma_k}{2\omega_k} \\ \dfrac{3(20\alpha + C_4)}{4\omega_k} \dfrac{g_{3kk}}{g_{1kk}} a_k & -\left(C_1 \dfrac{g_{0kk}}{g_{1kk}} \dfrac{1}{a_k} + \dfrac{3C_3}{4} \dfrac{g_{2kk}}{g_{1kk}} a_k \right) \dfrac{\sin \gamma_k}{2\omega_k} \\ + \left(-C_1 \dfrac{g_{0kk}}{g_{1kk}} \dfrac{1}{a_k^2} + \dfrac{3C_3}{4} \dfrac{g_{2kk}}{g_{1kk}} \right) \dfrac{\cos \gamma_k}{2\omega_k} & \end{bmatrix}_{(a_0, \gamma_0)}
$$

$$(47)$$

Jacobian eigenvalues for these points are found in order to determine their stability. Stability of steady-state solutions of a uniform microcantilever is presented in Sec. 6.1.

6. Uniform Microcantilever Resonators

The case of uniform cantilever beams is considered. The solution of the zero-order partial differential equation (28), along with boundary conditions, gives the mode shapes for a uniform cantilever[33] as follows

$$
\varphi_k(z) = -\{\cos(\sqrt{\omega_k}z) - \cosh(\sqrt{\omega_k}z) + C_k[\sin(\sqrt{\omega_k}z) - \sinh(\sqrt{\omega_k}z)]\}, \tag{48}
$$

where ω_k and C_k are dimensionless natural frequencies (ω^* in Eq. 24) and constant coefficients, respectively, given for the first five modes in Table 1. Substituting Eq. (48) into Eq. (37), the coefficients g_{1kk} and g_{3kk} for the first mode $(k = 1)$ and second mode $(k = 2)$ are obtained as follows

$$
\begin{aligned} g_{011} &= 0.7830; & g_{111} &= 1.0000; & g_{211} &= 1.4778; & g_{311} &= 2.3488 \\ g_{022} &= 0.4336; & g_{122} &= 1.0003; & g_{222} &= 0.4529; & g_{322} &= 1.7830. \end{aligned} \tag{49}
$$

Table 2 gives values of the physical characteristics of a typical microbeam.[17] They led to the values given in Table 3 of the dimensionless parameters of Eq. (23). Using

Table 1. First five natural frequencies and mode shape coefficients for uniform cantilever.

	$k = 1$	$k = 2$	$k = 3$	$k = 4$	$k = 5$
ω_k	3.51562	22.0336	61.70102	120.91202	199.85929
C_k	−0.734	−1.0185	−0.9992	−1.00003	−1.00000

Table 2. Physical characteristics of a microbeam.

Parameter	Symbol	Value
Beam width	W	$20\,\mu\mathrm{m}$
Beam length	l	$300\,\mu\mathrm{m}$
Beam thickness	h	$2.0\,\mu\mathrm{m}$
Initial gap distance	g	$8.0\,\mu\mathrm{m}$
Material density	ρ	$2330\,\mathrm{kg/m^3}$
Young's modulus	E	$169\,\mathrm{GPa}$
Quality factor	Q	350
Peak AC voltage	V_0	$12.5\,\mathrm{V}$

Table 3. Dimensionless system coefficients.

Dimensionless parameter	Symbol	Value
Casimir effect	α	2.9×10^{-9}
Amplitude of excitation	δ	0.10
Fringe correction	f	0.26
Damping coefficient	b^*	0.01

Table 3 and Eq. (49), the frequency−amplitude relationships of steady-states near-half natural frequency are obtained for both first mode ($k = 1$) and second mode ($k = 2$). It should be noted here that we are considering a resonator with physical dimensions on the micro-scale (Table 2). As a result, the parameter α tracking the influence of the Casimir force is extremely small compared to the other dimensionless parameters (Table 3). Therefore, the Casimir effect does not have an influence on the microcantilever resonator. The results presented in this section are for mode 1 ($k = 1$). The influence of the Casimir effect on a nanoresonator will be a point of future investigation.

6.1. *Steady-state solutions (MMS)*

Phase-amplitude differential Eqs. (42) and (43) are numerically integrated to observe the long-term behavior of the microresonator. Integration was carried out using the *Matlab* function *ode45*, which uses an explicit Runge−Kutta algorithm. The phase-amplitude behavior is obtained through numerical integration with the initial amplitude and phase equal to zero. Figure 2 illustrates the phase-amplitude response in time of the resonator with zero initial conditions. This figure illustrates the convergence to a steady-state solution of $a = 0.21$ amplitude, and $\gamma = 3.0$ phase. In addition, Fig. 3 shows the time−amplitude response of the resonator. As one can notice, the resonator reaches the steady-state amplitude of $a = 0.21$.

The steady-state amplitude−frequency response (Eqs. (45) and (46)) of the microresonator (Table 3) obtained using the MMS is illustrated in Figs. 4 and 5. The solid and dashed lines in Figs. 4 and 5 illustrate stable and unstable steady-state solutions, respectively. Figure 4 shows the steady-state frequency−amplitude response demonstrating a softening characteristic. The response consists of two

656   *D. I. Caruntu & M. W. Knecht*
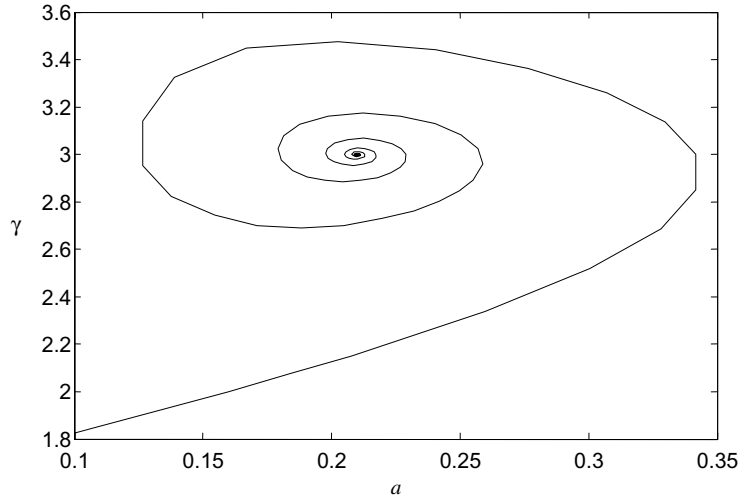
Fig. 2. Phase plot of a uniform cantilevered resonator tip showing a spiral trajectory to a fixed point representing the systems steady-state amplitude and phase for the first mode ($k = 1$). The phase plot was produced by integrating the MMS equations using the initial amplitude and phase of $a_0 = 0$ and $\gamma_0 = 0$, respectively. Dimensionless parameters: $\sigma = 0.02, \alpha = 0, \delta = 0.1, f = 0.26$, and $b^* = 0.01$.
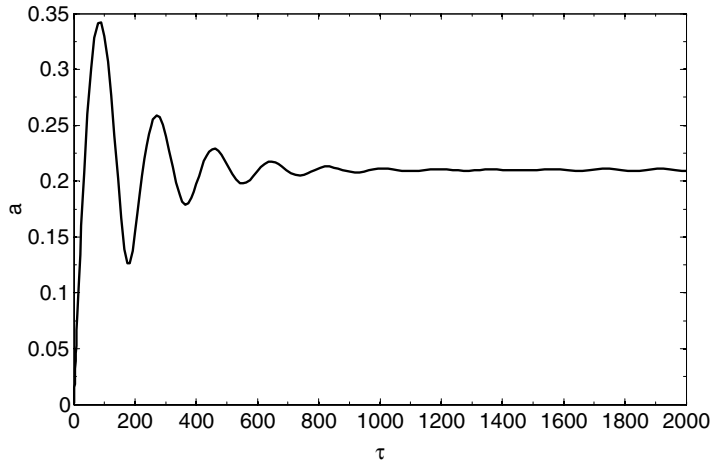

Fig. 3. Time response for a uniform cantilevered resonator tip using MMS for the first mode ($k = 1$). A steady-state amplitude of $a = 0.21$ is reached. The initial amplitude of the tip is $a_0 = 0$. Dimensionless parameters: $\sigma = 0.02, \alpha = 0, \delta = 0.1, f = 0.26$, and $b^* = 0.01$.

branches. The right-hand side branch represents stable solutions. The left-hand side branch consists of both stable (solid line) and unstable (dash line) solutions. A frequency sweep of the resonator from higher to lower frequencies (Fig. 4) leads to a smooth increase in the amplitude up to the gap length. In reality, before such large deflections can be reached, a pull-in phenomenon, which cannot be predicted by the
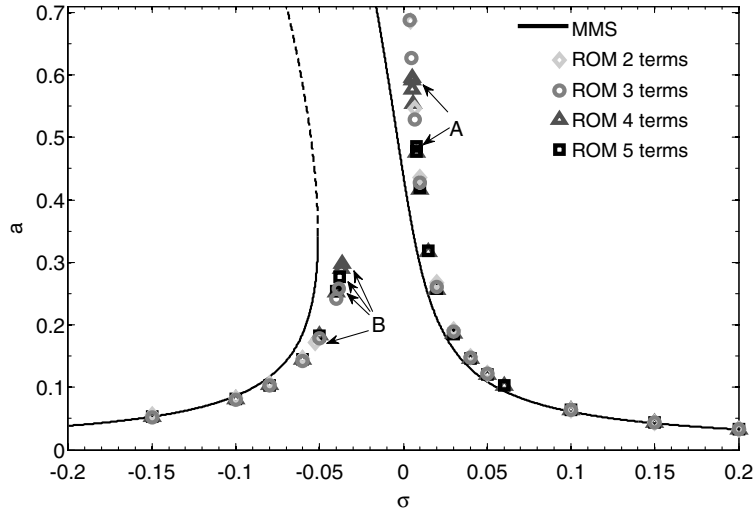
Fig. 4. Frequency response of a uniform capacitive resonator for mode 1 ($k =1$). The solid and dotted lines are solutions from the MMS representing stable and unstable points, respectively. The points are solutions using the ROM. A and B are where pull-in is predicted using the five-term ROM. Dimensionless parameters: $\alpha = 0$, $\delta = 0.1$, $f = 0.26$, and $b^* = 0.01$.
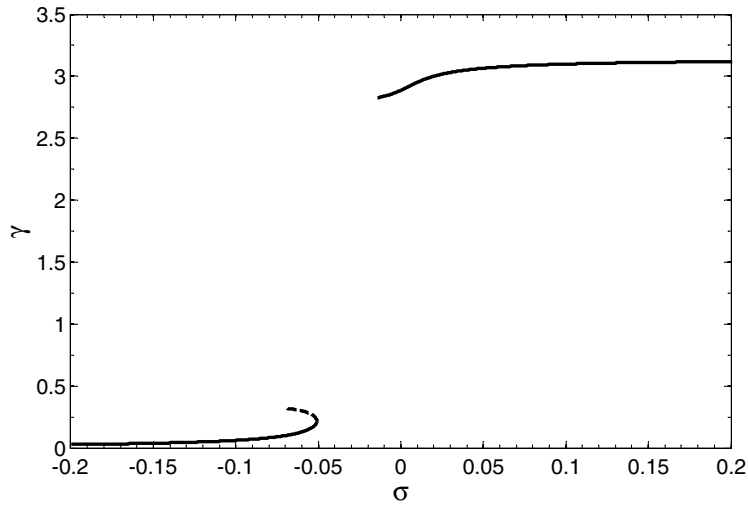
Fig. 5. Phase response of a uniform capacitive resonator for mode 1 ($k =1$). The solid and dashed lines are solutions from the MMS representing stable and unstable points, respectively. Dimensionless parameters: $\alpha = 0$, $\delta = 0.1$, $f = 0.26$, and $b^* = 0.01$.

MMS,[9] will occur. When the frequency is swept from lower frequencies to higher frequencies, the amplitude smoothly increases until unstable solutions along the left-hand side branch are reached (Fig. 4). At this point, a jump would occur to higher amplitudes, which results in a pull-in phenomenon. A similar behavior is found in

Ref. 9 for an electrically actuated clamped-clamped microbeam when parametrically excited at half its natural frequency. Figure 5 illustrates the phase-frequency response of the resonator. The lower branch represents the phase difference for amplitude solutions along the left-hand side branch of Fig. 4. The upper branch (Fig. 5) represents the phase difference for solutions along the right-hand side branch of Fig. 4. The response of the microbeam is nearly in phase with the excitation (phase difference is almost zero) for the stable steady-state solutions on the left-hand side branch of Fig. 4, and the lower part of the lower branch of Fig. 5. The phase difference between the resonator and excitation is nearly π in Fig. 5 for steady-state solutions along the right-hand side branch of Fig. 4, at higher frequencies $\sigma > 0.05$.

6.2. *Reduced-order model (ROM)*

A ROM method, based on the application of a Galerkin procedure that uses the undamped mode shapes of a cantilevered beam as the basis functions, was used for comparison with MMS results. In Eq. (22), the Casimir force was negligible, $\alpha \approx 0$ (Table 3). The ROM was constructed[13] by using a Galerkin procedure in which the solution is assumed as

$$u(z, \tau) = \sum_{i=1}^{N} u_i(\tau)\phi_i(z), \tag{50}$$

where the number of terms N was finite, $\phi_i(z)$ was a set of N linear undamped mode shapes of the uniform cantilever resonator, and $u_i(\tau)$ were time-dependant
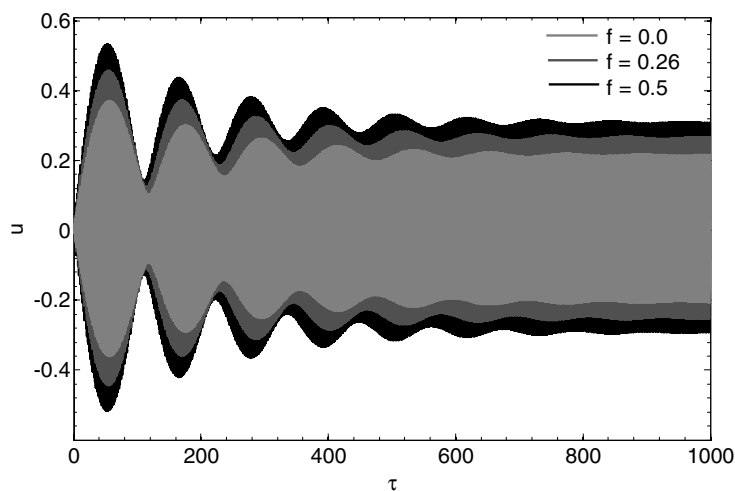
Fig. 6. Time response for the tip of a uniform cantilever resonator using ROM showing the influence of the fringe correction on the steady-state amplitude for mode 1 ($k = 1$). As the fringe correction parameter increases, the steady-state amplitude increases. The initial tip displacement is $u_0 = 0$. Dimensionless parameters: $\sigma = 0.02$, $\alpha = 0$, $\delta = 0.1$, and $b^* = 0.01$.

coefficients. The mode shapes $\phi_i(z)$ are given by Eq. (48). To implement this procedure, the equation of motion, Eq. (22) was multiplied by $(1 - u)^2$ to eliminate any displacement terms from appearing in the denominator.[25] Equations (48) and (50) were then substituted into the result. Next, multiplying by $\phi_n(z)$, and integrating the entire equation from $z = 0$ to 1, a system of N second-order equations in time resulted since $n = 1, 2, \ldots, N$. The system of equations was then integrated using *Matlab*. Steady states were found using two-, three-, four- and five-term ROMs for different values of the detuning parameter σ, and then plotted in Fig. 4. Figure 6 illustrates the motion of the cantilever tip as a function of time. It is noted that the time response of the resonator using the ROM and the time response predicted by the MMS in Fig. 3 show similar transient behavior before steady state is reached.

7. Discussion and Conclusions

The behavior of near-half natural frequency of an electrostatically actuated cantilever microresonator is investigated. The microresonator is modeled as an Euler−Bernoulli thin beam. Therefore, no nonlinearities arise from the structure itself. However, electrostatic and Casimir forces acting on the resonator induce parametric nonlinear resonances. Parametric coefficients are found in both linear and nonlinear terms within the governing equation. The model also includes first-order fringe correction of the electrostatic field.

An approach in which the MMS is directly applied to the partial differential equation of motion is used to find the frequency−amplitude relationship of the steady-state solutions of the system. Then, these solutions are compared with numerical results from the ROM. The frequency response of the system is illustrated in Figs. 4 and 5, in the case of a uniform microcantilever resonator (Table 3).

7.1. *Comparison of MMS and ROM results*

Although accurate for small amplitudes and weak nonlinearities, the MMS is limited. It cannot accurately predict frequencies and voltages at which pull-in phenomenon occurs. Nayfeh and Younis[9,10] reported the use of a ROM using a Galerkin procedure to predict periodic motions. Results were then compared to perturbation method. The Galerkin procedure was able to accurately capture the behavior of the system where the perturbation method could not,[25] i.e. for moderately large deflections up to the pull-in instability limit. Using three or more modes guarantees the convergence of the steady-state amplitude.[10,25] In the present work, similar two-, three-, four-, and five-term ROMs were used for the cantilever resonator. The results of the ROM were compared with the direct approach using MMS. Figure 4 shows a comparison between ROM and MMS for frequency−amplitude response. At larger amplitudes, the ROM solutions diverge from MMS. The MMS underestimates the steady-state amplitude at frequencies along the right-hand side branch in Fig. 4 and over-estimates the steady-state amplitude along the left-hand side branch. One can also

say that MMS overestimates the nonlinearities. MMS shows a stronger softening effect (branches are more bent to the left) than the ROM. When the amplitude is below 0.2, both methods coincide relatively well. This is expected since MMS is valid for only moderate to small deflections.

Regarding the number of terms in the ROM, the two-term ROM predicts the location of the right-hand side branch just as well as the five-term ROM (Fig. 4). The important difference between the lower-term ROMs and the higher-term ROMs is the ability to predict pull-in instability. For accurate predictions of pull-in, a sufficient number of terms must be used in the ROM model. The two- and three-term ROMs predicted dimensionless steady-state amplitudes and dimensionless deflections of the resonator's tip exceeding unity, but not a pull-in phenomenon. Dimensionless amplitudes (21) cannot exceed unity since the dimensional amplitudes cannot exceed the gap between the microcantilever and ground plate. Numerical simulations conducted in this research demonstrate that four or more terms are required for the ROM to predict pull-in. Figure 4 illustrates the numerical convergence process (from two-term ROM to five-term ROM) of finding the pull-in amplitude. The points labeled A in Fig. 4 show where the four- and five-term ROMs predict the pull-in. The 5-term ROM predicts more accurately the pull-in phenomenon. As the excitation frequency is swept downward along the right-hand side stable branch, the pull-in occurs at $\sigma = 0.008$, point labeled A in Fig. 4. As the excitation frequency is swept upward along the left-hand side branch, point B in Fig. 4, where the resonator becomes unstable resulting in a pull-in phenomenon is reached.

Pull-in manifests itself as a sudden increase in resonator tip velocity toward the underlying substrate as the tip reaches its maximum displacement (Figs. 7(a) and 7(b)). This leads to contact between the resonator and ground plate. When this occurs, the numerical solution changes so rapidly that the code used to model

(a)
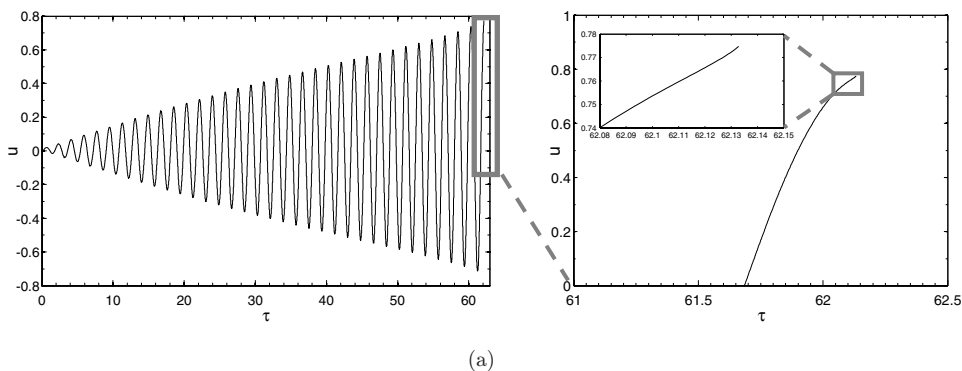
Fig. 7. (a) Time response of the resonator tip's displacement illustrating the occurance of pull-in phenonena using the five-term ROM (b) Time response of the resonator tip's velocity illustrating the occurrence of pull-in phenomena using the five-term ROM. Dimensionless parameters: $\alpha = 0$, $b^* = 0.01$, $f = 0.26$, $\delta = 0.1$, and $\sigma = -0.03$.
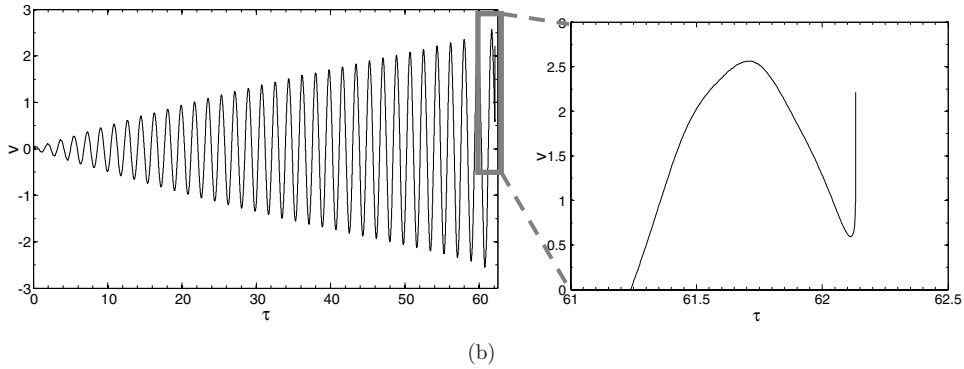
(b)

Fig. 7. (*Continued*)

the system is unable to continue. Figures 7(a) and 7(b) illustrate the pull-in phenomenon showing how the resonator looses stability. The dimensionless velocity v in Fig. 7(b) suddenly increases while the dimensionless deflection u in Fig. 7(a) of the resonator tip approaches unity. There is an inflection in the displacement plot, the concavity changes from concave down to concave up as the cantilever tip begins to move toward pull-in. It is important to note than both methods MMS and ROM predict the same system behavior for smaller amplitudes. The ROM is more accurate for larger deflections. The increased accuracy comes at a cost, though. First, the ROM is more costly in the form of computational time (CPU time). Each point of the five-term ROM in Fig. 4 represents almost an hour of CPU time on a 2.70-GHz Dual Core PC processor with 4-GB RAM, where as the MMS plot in the same figure was plotted in minutes. The MMS is computationally more efficient than methods using direct numerical integration.[35] Second, numerical methods such as the ROM have a problem of not providing an insight into the underlying physics and interactions of a system.[36] An analytical approach, such as the MMS, allows for a better insight of the dependence of the system on its various parameters, and has the ability to predict interesting phenomena.

Figure 8 compares the influence of the excitation parameter δ on the frequency response predicted by both methods MMS and ROM. Even though the MMS is limited to weak nonlinearities with only moderate displacements, if one is interested in modeling general system behavior without need to identify exact instability points, the MMS method seems to be suitable. Using analytical methods in conjunction with numerical methods can be a powerful way to study system behavior, particularly in structural dynamics. Although there is a significant difference in the predictions of MMS and ROM for amplitudes greater than $a = 0.1$, both methods are in good agreement. Since a micro-scale resonator is being considered, the Casimir force is negligible; therefore, the only nonlinear influence on the system is the electrostatic excitation. The strength of the nonlinearities in the system is controlled by the excitation parameter δ. A decrease in its value weakens the nonlinearities in the
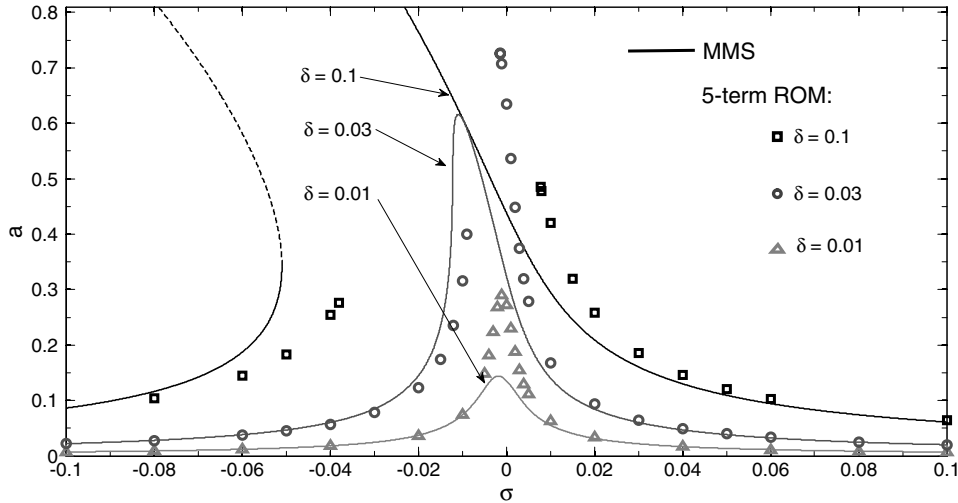
662   *D. I. Caruntu & M. W. Knecht*

Fig. 8. Comparison of the frequency response for a uniform cantilevered resonator using the ROM and MMS showing the influence of the dimensionless excitation parameter δ for the first mode ($k = 1$). Dimensionless parameters: $\alpha = 0$, $f = 0.26$, and $b^* = 0.01$.

system. Both the ROM and MMS predict this nonlinear weakening as illustrated in Fig. 8. At smaller values of the excitation parameter δ, the two methods are in very good agreement. There is significant variation in the two methods around the resonant peak at values of the excitation parameter $\delta = 0.01$ and 0.03. The ROM also predicts the resonant peak to split into two distinct branches at small values of the excitation parameter δ.

7.2. *Influence of parameters*

Influences of parameters b^*, δ, and f on the microresonator's response, first mode ($k = 1$), are discussed next. Figures 9 and 10 illustrate the influence of damping b^* on the frequency response of the resonator. One can notice from Fig. 9 that the frequency response on the steady-state amplitude is unaffected by changes in damping for low damping values (Fig. 9). Frequency responses are nearly identical for damping coefficients $b^* = 0.01$ and $b^* = 0.001$. When the damping coefficient grows sufficiently large, the two branches merge and produce a standard resonance peak with a slight softening characteristic. At frequencies away from the resonant peak, the damping does not affect the steady-state amplitude. All three frequency response curves in Fig. 9 coincide. For example, at $\sigma = 0.03$, all three plots in the amplitude−frequency curve have the same amplitude of $a \approx 0.2$. The phase γ of the resonator with respect to the excitation frequency is only marginally effected by damping as illustrated in Fig. 10. When the damping is lower, there are two distinct branches in the phase plot. As the damping increases, these branches merge such that there is a smooth transition of the phase from lower to higher frequencies.
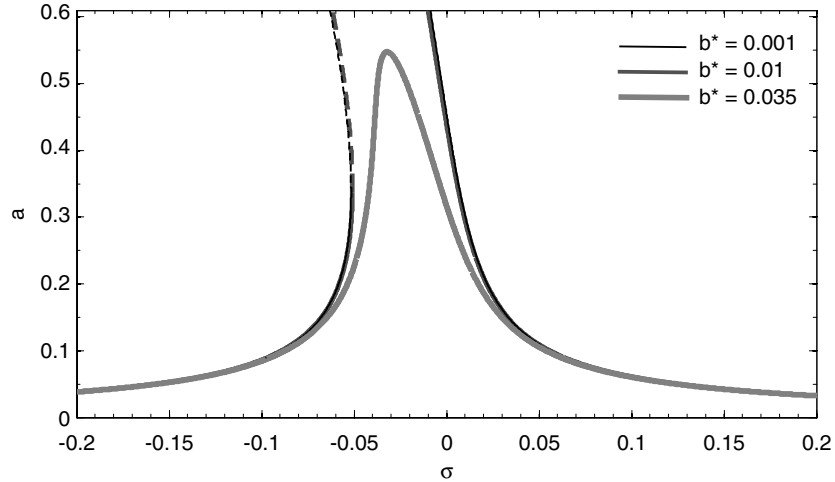
Fig. 9. Frequency response of a uniform cantilevered resonator using the MMS showing the influence of the dimensionless damping parameter b^* for the first mode ($k = 1$). Dimensionless parameters: $\alpha = 0$, $\delta = 0.1$, and $f = 0.26$.
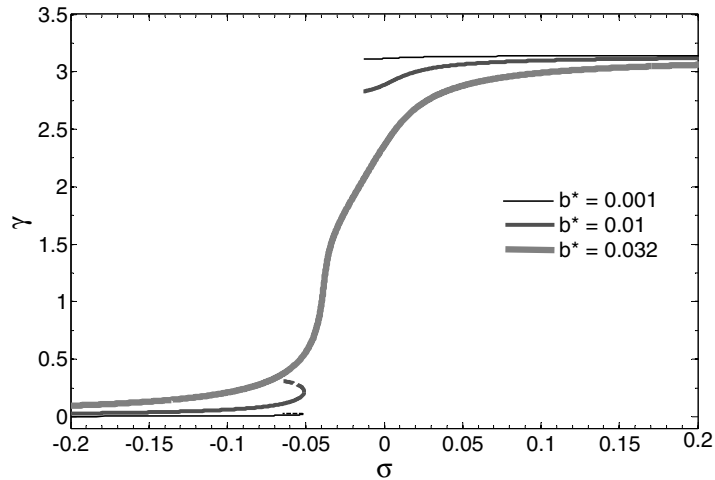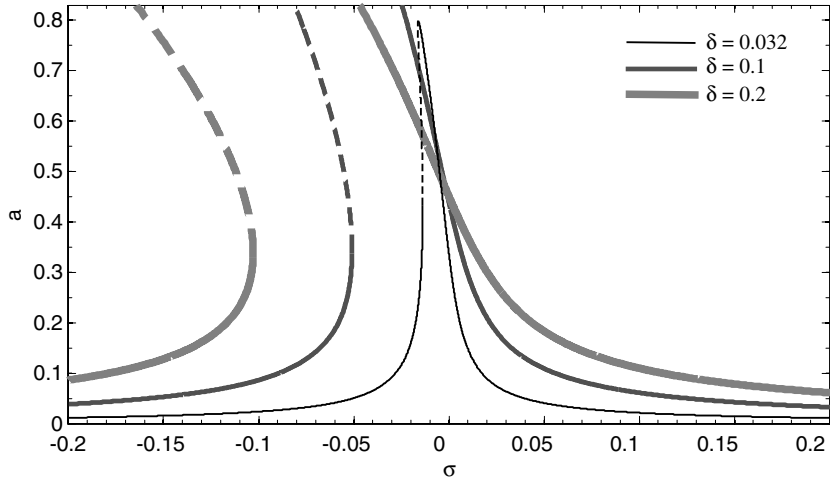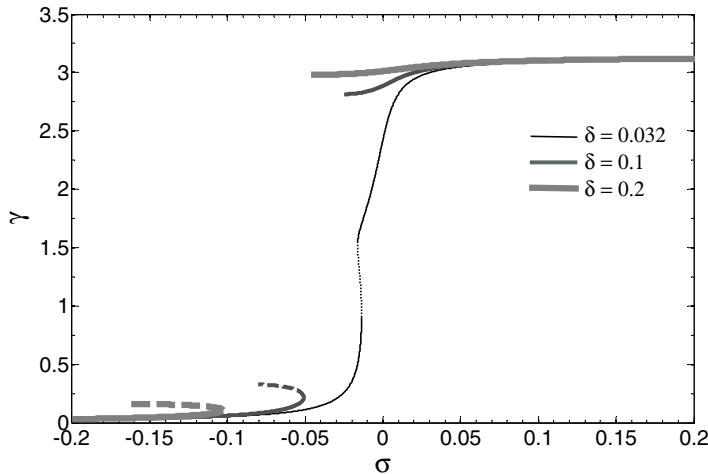

Fig. 10. Phase response of a uniform cantilevered resonator using the MMS showing the influence of the dimensionless damping parameter b^* for the first mode ($k = 1$). Dimensionless parameters: $\alpha = 0$, $\delta = 0.1$, and $f = 0.26$.

Figures 11 and 12 illustrate the influence of the dimensionless excitation parameter δ on the frequency response of the system. At lower excitation forces, the nonlinear behavior of the system is not evident (Fig. 11). As δ is increased, the influence of the nonlinearities becomes more obvious showing a typical softening characteristic. As δ continues to increase, the frequency−amplitude curve splits into two distinct branches where the left-hand side branch is unstable at frequencies, as

Fig. 11. Frequency response of a uniform cantilevered resonator using the MMS showing the influence of the dimensionless excitation parameter δ for the first mode ($k = 1$). Dimensionless parameters: $\alpha = 0$, $f = 0.26$, and $b^* = 0.01$.

Fig. 12. Phase response of a uniform cantilevered resonator using the MMS showing the influence of the dimensionless excitation parameter δ for the first mode ($k = 1$). Dimensionless parameters: $\alpha = 0$, $f = 0.26$, and $b^* = 0.01$.

indicated by the dash line in Fig. 11, and the right-hand side branch is stable. The formation of the branches is further illustrated in Fig. 13, where at small excitations, the two solutions to the parametric equations (45) and (46) are showed as upper and lower curves. The lower curve represents solutions when the sign is negative in Eq. (46) and the upper curve represents solutions when the sign is positive. As the excitation parameter is increased, it is seen that the lower curve gets pulled upward
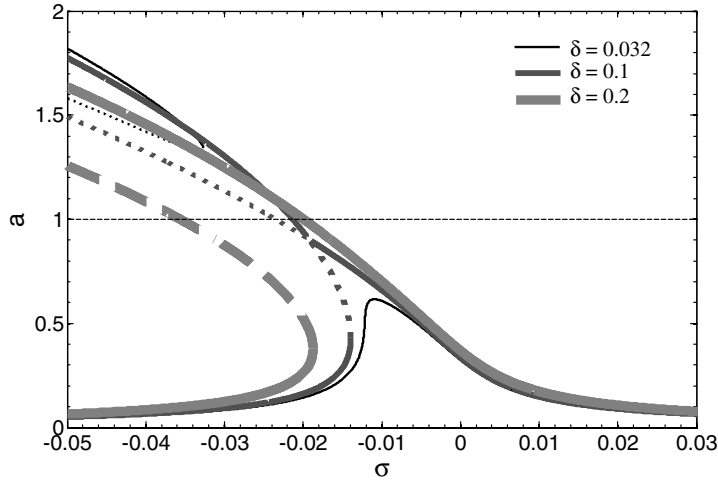
Fig. 13. Frequency response of a uniform cantilevered resonator showing the two solutions from Eq. (49) developed using the MMS for the first mode ($k = 1$). As the dimensionless excitation parameter δ increases, upper and lower branches merge. Dimensionless parameters: $\alpha = 0$, $f = 0.26$, and $b^* = 0.01$.

while the lower curve gets pulled downward. The formation of the two branches at larger excitation forces occurs when the curves representing the two solutions merge. It should be noted that the amplitudes represented by the upper curve are at values larger than unity and hence have no physical meaning since the dimensionless beam deflection cannot be larger than one (21). At most frequencies, it is seen that increased excitation forces result in an increase in the steady-state amplitude as expected. At frequencies just below the systems half-natural frequency ($\sigma \approx -0.01$), the system behavior is different (Fig. 11). Within a narrow band of frequencies between $\sigma = -0.01$ and $\sigma = -0.025$, the steady-state amplitude decreases with increasing the excitation parameter. The frequency response of the resonators phase γ is illustrated in Fig. 12 for different excitation parameters. The phase has two distinct branches at higher excitation parameters (Fig. 12). The upper and lower branches in Fig. 12 are associated with the right- and left-hand side branches in Fig. 11, respectively. The phase is unaffected by the change in excitation parameter δ for frequencies outside the interval $\sigma = -0.01$ and $\sigma = -0.025$. Outside this interval, the phase γ is about π and zero (Fig. 12) for steady states on the right- and left-hand side branches of Fig. 11, respectively. As the excitation parameter δ is decreased, the nonlinear effect reduces and the two branches merge (Fig. 12).

Figures 14 and 15 show the effect of the fringe parameter f on the frequency response of the resonator. It should be first noted that f is directly related to the how narrow the microbeam is compared to the gap (23). Hence, narrower beams will experience larger fringe effect. The frequency response of the amplitude (Fig. 14), shows that increasing the fringe parameter has the effect of shifting the branches to lower frequencies. The left-hand side branch is more affected. Figure 15 shows that
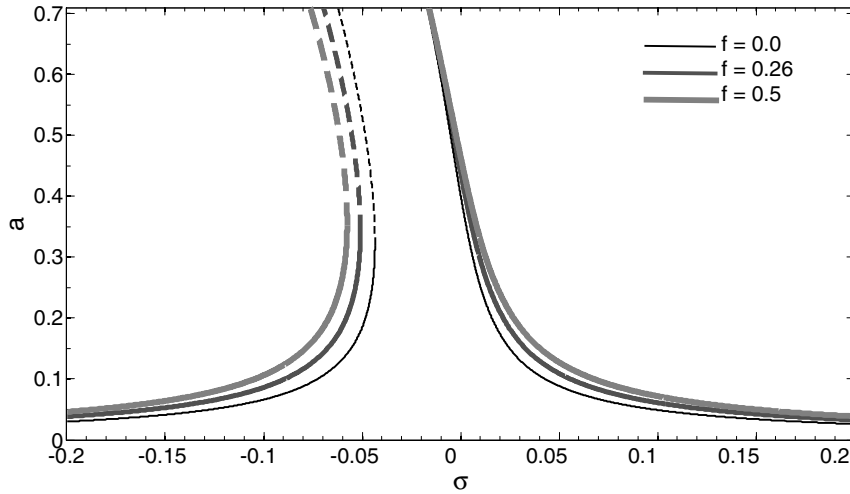
Fig. 14. Frequency response of a uniform cantilevered resonator using the MMS showing the influence of the fringe correction for the first mode ($k = 1$). Dimensionless parameters: $\alpha = 0$, $\delta = 0.1$, and $b^* = 0.01$.
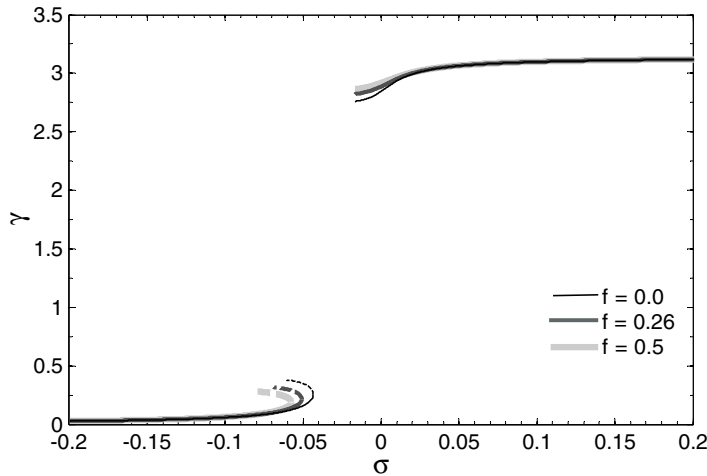

Fig. 15. Phase response of a uniform cantilevered resonator using the MMS showing the influence of the fringe correction for the first mode ($k = 1$). Dimensionless parameters: $\alpha = 0$, $\delta = 0.1$, and $b^* = 0.01$.

the fringe correction f has no significant effect on the frequency response of the phase γ for either branch in Fig. 4. Figure 6 illustrates the influence of the fringe factor f on resonator's amplitude using ROM. This is in good agreement with MMS (Fig. 14).

Next, the influences of parameters b^*, δ, and f on the microresonator response, for excitation frequencies near half of the second natural frequency ($k = 2$) (Table 1), are discussed. Figures 16 and 17 show that the influence of damping on the response of the system is similar to what was seen in the first mode although there are two
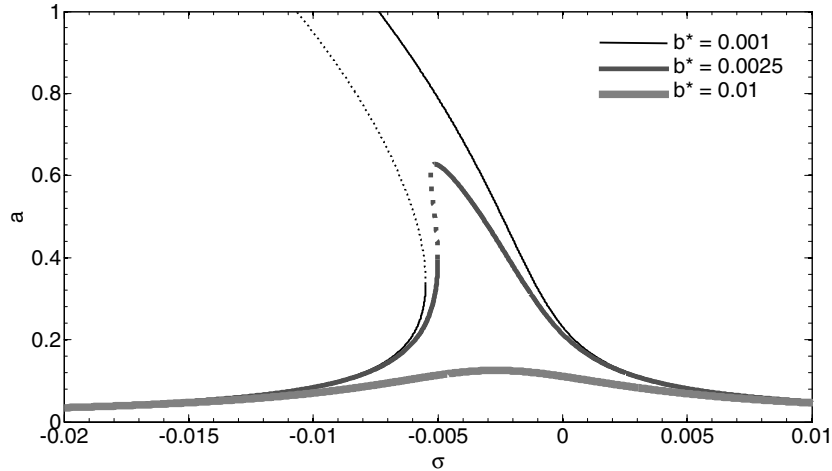
Fig. 16. Frequency response of a uniform cantilevered resonator using the MMS showing the influence of the dimensionless damping parameter b^* for the second mode ($k = 2$). Dimensionless parameters: $\alpha = 0$, $\delta = 0.1$, and $f = 0.26$.
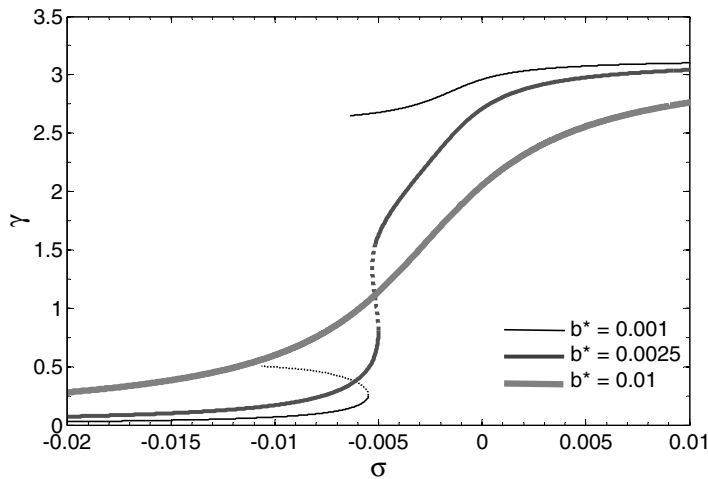

Fig. 17. Phase response of a uniform cantilevered resonator using the MMS showing the influence of the dimensionless damping parameter b^* for the second mode ($k = 2$). Dimensionless parameters: $\alpha = 0$, $\delta = 0.1$, and $f = 0.26$.

differences. The first difference is that in order for resonance to occur with significant amplitude, the damping must be greatly reduced. One could notice in Fig. 16 how the damping coefficient used for half of the first natural frequency ($b^* = 0.01$) produces almost no resonant response. A resonant response is not seen unless the damping is significantly reduced. One can notice that for the second mode a damping parameter of $b^* = 0.001$ was used (where $b^* = 0.01$ was used for first

mode). The second difference is that a resonant response occurs over a much narrower band of frequencies than with the first mode. A comparison between the scales of the detuning parameter σ on the frequency response plots for the second and first modes shows that the values of σ are a factor of 10 smaller for the second mode.

Figures 18 to 19 are the frequency response of the resonator showing the influence of the fringe parameter f. Figures 20 to 21 illustrate the influence of the excitation
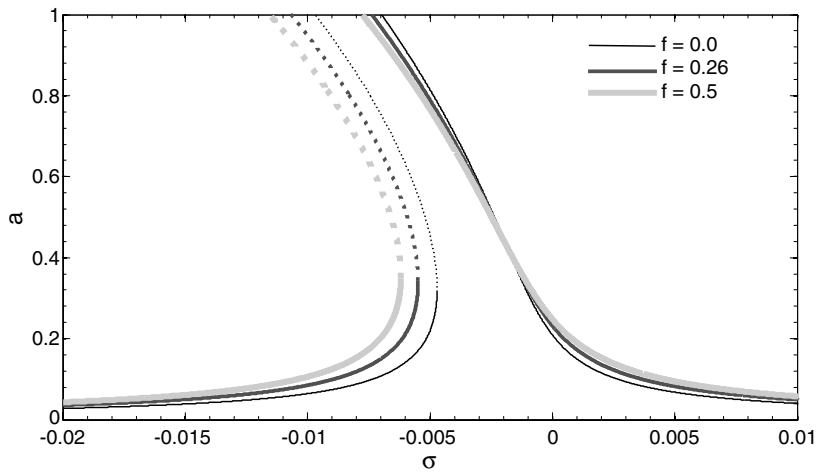
Fig. 18. Frequency response of a uniform cantilevered resonator using the MMS showing the influence of the fringe correction for the second mode ($k = 2$). Dimensionless parameters: $\alpha = 0$, $\delta = 0.1$, and $b^* = 0.001$.
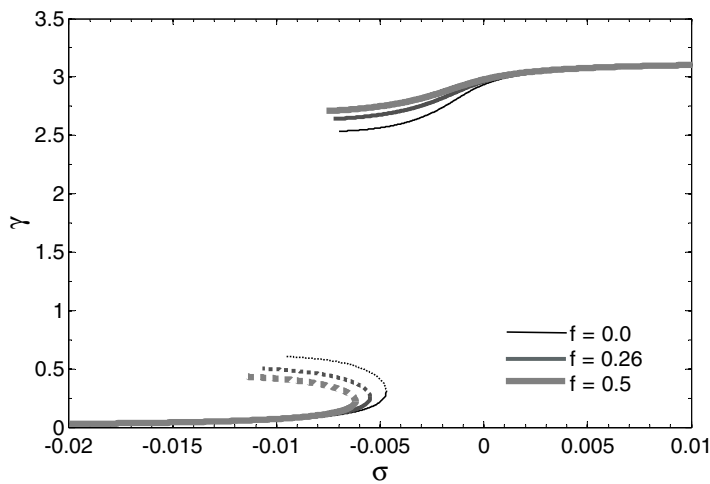

Fig. 19. Phase response of a uniform cantilevered resonator using the MMS showing the influence of the fringe correction for the second mode ($k = 2$). Dimensionless parameters: $\alpha = 0$, $\delta = 0.1$, and $b^* = 0.001$.
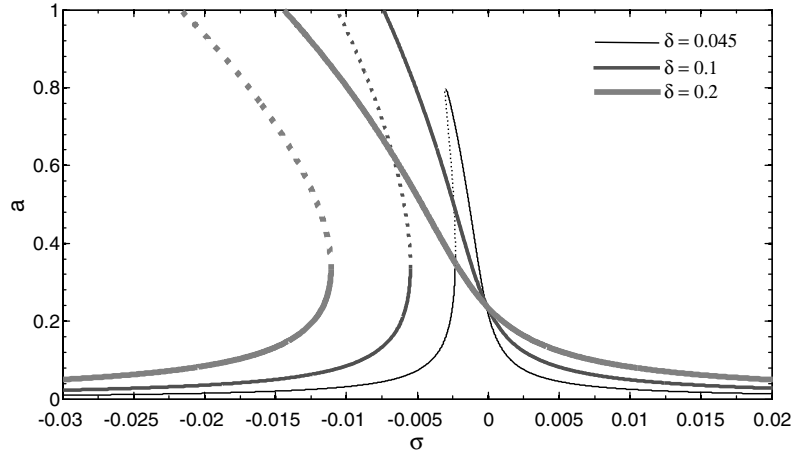
Fig. 20. Frequency response of a uniform cantilevered resonator using the MMS showing the influence of the dimensionless excitation parameter δ for the second mode ($k = 2$). Dimensionless parameters: $\alpha = 0$, $f = 0.26$, and $b^* = 0.001$.
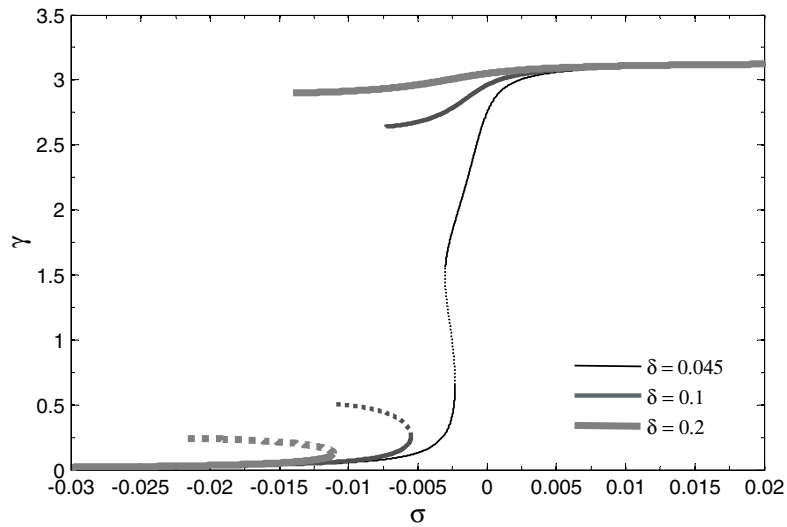

Fig. 21. Phase response of a uniform cantilevered resonator using the MMS showing the influence of the dimensionless excitation parameter δ for the second mode ($k = 2$). Dimensionless parameters: $\alpha = 0$, $f = 0.26$, and $b^* = 0.001$.

parameter δ. The influence of these parameters on the resonator in the second mode is nearly the same as what was seen in the first mode.

7.3. *Model limitations*

By using the Euler−Bernoulli theory, the model is limited to long and thin beams in which a length−thickness ratio (ℓ/h) of 10 for the first mode,[37] or 100 or greater

for any mode, are typically considered. The mode at which the beam is excited also affects the validity of the Euler−Bernoulli theory. At modes beyond the primary ($k = 1$), the accuracy of the theory is questionable.[37] The use of the Palmer approximate formula for a fringe correction to the electrostatic force (9) allows the model to be accurate for narrower beams than the traditional parallel plate model (3). A width−thickness ratio greater than 5 and width−gap ratio greater than 10 are reasonably accurate for the Palmer field correction.[21]

References

1. A. Ramezani, A. Alasty and J. Akbari, Closed-form solutions of the pull-in instability in nano-cantilevers under electrostatic and intermolecular surface forces, *International Journal of Solids and Structures* **44** (2007) 4925−4941.
2. A. Ramezani, A. Alasty and J. Akbari, Analytical investigation and numerical verification of Casimir effect on electrostatic nano-cantilevers, *Microsystem Technologies* **14** (2008) 145−157.
3. J. F. Rhoads, S. W. Shaw, K. L. Turner, J. Moehlis, B. E. DeMartini and W. Zhang, Generalized parametric resonance in electrostatically actuated microelectromechanical oscillators, *Journal of Sound and Vibration* **296** (2006) 797−829.
4. W. Zhang and K. L. Turner, Application of parametric resonance amplification in a single-crystal silicon micro-oscillator based mass sensor, *Sensors and Actuators A* **122** (2005) 23−30.
5. W. Zhang, R. Baskaran and K. L. Turner, Effect of cubic nonlinearity on auto-parametrically amplified resonant MEMS mass sensor, *Sensors and Actuators A* **102** (2002) 139−150.
6. H. Yabuno and H. Kaneko, Van der Pol type self-excited micro-cantilever probe of atomic force microscopy, *Journal of Nonlinear Dynamics* **54** (2008) 137−149.
7. K. M. Cheng, Z. Weng, D. R. Oliver, D. J. Thomson and G. E. Bridges, Microelectromechanical resonator characterization using noncontact parametric electrostatic excitation and probing, *Journal of Microelectromechanical Systems* **16**(5) (2007) 1054−1060.
8. J. F. Rhoads and S. W. Shaw, Tunable microelectomechanical filters that exploit parametric resonance, *Journal of Vibration and Acoustics* **127**(5) (2005) 423−430.
9. A. H. Nayfeh and M. I. Younis, Dynamics of MEMS resonators under superharmonic and subharmonic excitations, *Journal of Micromechanics and Microengineering* **15** (2005) 1840−1847.
10. A. H. Nayfeh, M. I. Younis and E. M. Abdel-Rahman, Dynamic pull-in phenomenon in MEMS resonantors, *Nonlinear Dynamics* **48** (2007) 153−163.
11. E. M. Abdel-Rahman, M. I. Younis and A. H. Nayfeh, Finite-amplitude motions of resonators and their stability, *Journal of Computational and Theoretical Nanoscience* **4** (2004) 385−391.
12. M. I. Younis and A. H. Nayfeh, A study of the nonlinear response of a resonant microbeam to an electric actuation, *Nonlinear Dynamics* **31** (2003) 91−117.
13. F. M. Alsaleem, M. I. Younis and H. M. Ouakad, On the nonlinear resonances and dynamic pull-in of electrostatically actuated resonators, *Journal of Micromechanics and Microengineering* (2009) 14.
14. B. E. DeMartini, H. E. Butterfield, J. Moehlis and K. L. Turner, Chaos for a microelectromechanical oscillator governed by the nonlinear mathieu equation, *Journal of Microelectromechanical Systems* **16**(6) (2007) 1314−1323.

15. M. F. Daqaq, C. Stabler, Y. Qaroush and T. Seuaciuc-Osorio, Investigation of power harvesting via parametric excitations, *Journal of Intelligent Material Systems and Structures* **20** (2009) 545−557.

16. K. Changkong, Resonant pull-in of a double-sided driven nanotube-based electro-mechanical resonator, *Journal of Applied Physics* **105**(024301) (2009) 1−8.

17. M. M. Zand and M. T. Ahmadian, Vibrational analysis of electrostatically actuated microstructures considering nonlinear effects, *Communications Nonlinear Science and Numerical Simulation* **14** (2009) 1664−1678.

18. M. T. Ahmadian, H. Borhan and E. Esmailzadeh, Dynamic analysis of geometrically nonlinear and electrostatically actuated micro-beams, *Communications in Nonlinear Science and Numerical Simulation* **14** (2009) 1627−1645.

19. S. A. Emam, M. E. Khater and E. H. Gad, A static and nonlinear dynamic analysis of resonant microbeams, *Proceedings of the ASME 2007 International Design Engineering Technical Conferences & Computers and Information in Engineering Conference* (Las Vegas, NV, September 4−7, 2007).

20. S. Chaterjee and G. Pohit, A large deflection model for the pull-in analysis of electro-statically actuated microcantilever beams, *Journal of Sound and Vibration* **322** (2009) 396−986.

21. R. Batra, M. Porfiri and D. Spinello, Electromechanical model of electrically actuated narrow microbeams, *Journal of Microelectromechanical Systems* **15**(5) (2006).

22. H. B. Palmer, Capacitance of a parallel-plate capacitor by the Schwartz-Christoffel transformation, *Transaction of the American Institute Electrical Engineers* **56**(3) (1937) 363−366.

23. N. V. D. Meijs and J. T. Fokkema, VLSI circuit reconstruction from mask topology, *Integration* **2**(2) (1984) 85−119.

24. S. Krylov and S. Seretensky, Higher order correction of electrostatic pressure and its influence on the pull-in behavior of microstructures, *Journal of Micromechanics and Microengineering* **16** (2006) 1382−1396.

25. M. I. Younis, E. M. Abdel-Rahman and A. Nayfeh, A reduced-order model for electrically actuated microbeam-based MEMS, *Journal of Microelectromechanics Systems* **12**(5) (2003) 672−680.

26. M. Mojahedi, M. Moghimi Zand and M. T. Ahmadian, Static pull-in analysis of elec-trostatically actuated microbeams using homotopy perturbation method, *Applied Mathematical Modelling* **34** 1032−1041.

27. M. Boa and H. Yang, Squeeze film air damping in MEMS, *Sensors and Actuators A* **136** (2007).

28. H. Okada, T. Itoh and T. Suga, Wafer level sealing characterization method using Si micro cantilevers, *Sensors and Actuators A* **147** (2008) 359−364.

29. F. R. Blom, S. Bouwstra, M. Elwenspoek, J. H. J. Fluitman, Dependence of the quality factor of micromachined silicon beam resonators on pressure and geometry, *Journal of Vacuum Science and Technology B* **10**(1) (1992) 19−26.

30. H. Hosaka, I. Kiyoshi and S. Kuroda, Damping characteristic of beam-shaped micro-oscillators, *Sensors and Actuators A* **49** (1995) 87−95.

31. J. A. Pelesko and D. H. Bernstein, *Modeling MEMS and NEMS* (Chapman and Hall/ CRC, New York, NY, 2003).

32. S. K. Lamoreaux, The casimir force: Background, experiments, and applications, *Reports on the Progress of Physics* **68** (2005) 201−236.

33. S. Timoshenko, D. H. Young and Jr., W. Weaver, *Vibration Problems in Engineering* (fourth Edition) (John Wiley & Sons, New York, 1974).

34. D. Caruntu, Dynamic modal characteristics of transverse vibrations of cantilevers of parabolic thickness, *Mechanics Research Communications* **33**(3) (2008) 391−404.
35. B. Moon and B. Kang, Vibration analysis of harmonically excited non-linear system using the method of multiple scales, *Journal of Sound and Vibration* **263** (2003) 1−20.
36. R. Khanin, M. Cartmell and A. Gilbert, A computerized implementation of the multiple scales perturbation method using Mathematica, *Computers and Structures* **76** (2000) 565−575.
37. A. Labuschagne, N. F. J. van Renburg and A. J. van der Merwe, Comparison of linear beam theories, *Mathematical and Computer Modelling* **49** (2009) 20−30.